

Journal of Biomedical Optics

SPIEDigitalLibrary.org/jbo

Prehistological evaluation of benign and malignant pigmented skin lesions with optical computed tomography

Athanasios Kokolakis
Giannis Zacharakis
Konstantin Krasagakis
Konstantinos Lasithiotakis
Rosy Favicchio
George Spiliopoulos
Elpida Giannikaki
Jorge Ripoll
Androniki Tosca

Prehistological evaluation of benign and malignant pigmented skin lesions with optical computed tomography

Athanasios Kokolakis,^a Giannis Zacharakis,^c Konstantin Krasagakis,^a Konstantinos Lasithiotakis,^a Rosy Favicchio,^c George Spiliopoulos,^c Elpida Giannikaki,^b Jorge Ripoll,^c and Androniki Tosca^a

^aUniversity of Crete, University Hospital of Heraklion, Pigmented Lesion and Melanoma Clinic, Department of Dermatology, 71110, Voutes, Heraklion, Crete, Greece

^bUniversity of Crete, University Hospital of Heraklion, Medical School of Heraklion, Department of Pathology, 71110, Voutes, Heraklion, Crete, Greece

^cInstitute of Electronic Structure and Laser, Foundation for Research and Technology – Hellas (FORTH), N. Plastira 100, 70013, Vassilika Vouton, Heraklion, Crete, Greece

Abstract. Discrimination of benign and malignant melanocytic lesions is a major issue in clinical dermatology. Assessment of the thickness of melanoma is critical for prognosis and treatment selection. We aimed to evaluate a novel optical computed tomography (optical-CT) system as a tool for three-dimensional (3-D) imaging of melanocytic lesions and its ability to discriminate benign from malignant melanocytic lesions while simultaneously determining the thickness of invasive melanoma. Seventeen melanocytic lesions, one hemangioma, and normal skin were assessed immediately after their excision by optical-CT and subsequently underwent histopathological examination. Tomographic reconstructions were performed with a back-propagation algorithm calculating a 3-D map of the total attenuation coefficient (AC). There was a statistically significant difference between melanomas, dysplastic nevi, and non-dysplastic nevi, as indicated by Kruskal-Wallis test. Median AC values were higher for melanomas compared with dysplastic and non-dysplastic nevi. No statistically significant difference was observed when thickness values obtained by optical-CT were compared with histological thickness using a Wilcoxon signed rank test. Our results suggest that optical-CT can be important for the immediate prehistological evaluation of biopsies, assisting the physician for a rapid assessment of malignancy and of the thickness of a melanocytic lesion.

© 2012 Society of Photo-Optical Instrumentation Engineers (SPIE). [DOI: 10.1117/1.JBO.17.6.066004]

Keywords: optical computed tomography; prehistological evaluation; 3-D imaging, melanoma; melanocytic nevi; pigmented skin lesions; attenuation coefficient.

Paper 11797 received Dec. 30, 2011; revised manuscript received Mar. 31, 2012; accepted for publication Apr. 6, 2012; published online Jun. 4, 2012.

1 Introduction

Melanoma is a malignant tumor derived from melanocytes, which are found predominantly in the skin and are responsible for the production of the dark pigment melanin. It is more common in fair-skinned populations and is responsible for the majority of skin-cancer-related deaths.¹⁻⁴ The clinical progression of the patients suffering from skin melanoma is directly associated with the early diagnosis of the tumor. Although the prognosis of patients with early thin melanomas is favorable after sufficient surgical excision, when metastases occur, melanoma is incurable with high mortality rate.^{2,5}

Dysplastic nevi are benign melanocytic nevi, which are clinically atypical with irregular outline and a variegated appearance and are histologically characterized by architectural disorder and cytological atypia. Their significance in relation to melanoma is high since they can be considered stimulants of melanoma and markers of individuals at increased risk of developing melanoma. They are also potentially and occasionally actual precursors of melanoma. Morphologically and biologically, they are intermediate between common nevi and melanoma. The presence of dysplastic nevi in patients may mean deficient DNA repair and association with overexpression of pheomelanin,

which may lead to increased oxidative damage and increased danger for DNA damage and tumor progression.^{1,6-10}

The discrimination between malignant and benign melanocytic lesions is one of the major issues of clinical dermatology. Clinical studies report that the diagnosis by simple inspection has sensitivity 65 to 80%, depending on dermatologist experience, whereas dermoscopy increases this rate by approximately 20%, but is also dependent on the experience and training of the clinician.¹¹⁻¹⁵ In addition, the assessment of the depth of invasive melanoma is an important issue of clinical dermatology and essential for the determination of the prognosis and the selection of the suitable treatment. The necessity for improvement of the diagnostic accuracy of melanocytic lesions led to the development of imaging methods such as *in vivo* confocal laser scanning microscopy,¹⁶⁻²⁵ high-resolution ultrasound (U/S),²⁶⁻²⁹ spectroscopy,³⁰⁻³³ and optical coherence tomography (OCT),^{29,34-37} but none of them has gained wide acceptance as a diagnostic tool so far. Recently, an optical method using second harmonic generation imaging of collagen was investigated for demarcation of melanoma borders, without offering detailed and accurate evidence for the discrimination of the malignant from benign melanocytic lesions.³⁸

Herein, we present our initial results of a novel, non-contact diagnostic technique for three-dimensional (3-D) imaging of melanocytic lesions, using optical computed tomography

Address all correspondence to: Athanasios Kokolakis, University Hospital of Heraklion, Department of Dermatology, 71110, Voutes, Heraklion, Crete, Greece. Tel.: +30 2810 392429; Fax: +30 2810 392429; E-mail: a.kokolakis@med.uoc.gr

(optical-CT), in order to discriminate melanoma from benign nevi and determine the thickness of invasive melanoma.³⁹ This method is based on non-contact measurements of biopsy samples using diffused light illumination and multiple angle detection of transmitted light.^{40,41} A filtered back-projection algorithm was employed to calculate 3-D maps of the optical properties of the tissue samples. These maps were used for determining the depth and the type of lesion, with high accuracy and compared on a double-blind basis with histology. Based on the difference of the obtained optical properties, benign from malignant lesions could be consistently differentiated. To our knowledge, this is the first time that an appropriately adapted optical-CT method is applied to excised tissue samples without optical clearing or any kind of chemical fixation or alteration of the biopsies, in contrast with previous work.⁴²⁻⁴⁴ The value of developing such a method could be high for the treatment of melanoma, assisting the physician for a rapid evaluation of a melanocytic lesion and of its thickness. The treatment would be finalized after definitive histological results.⁴⁵

2 Materials and Methods

2.1 Experimental Setup

The optical-CT system developed for this study provides non-contact multiple-angle measurements of biopsy samples in order to calculate 3-D maps of their optical properties.^{46,47} The principle of the system is depicted schematically in Fig. 1. The light source was a white light lamp consisting of 80 light-emitting diode (LEDs). A diffuser was placed between the light source and the optical components directing the light onto the sample. Diffuse light was preferred rather than collimated laser beam for homogeneous illumination and for acquiring average values of the optical properties. The light was then reflected by a flat mirror, and it was guided to a linear polarizer (Hoya, Japan). After transmission through the sample, which was positioned on a rotational stage (Standa, Lithuania) covering 360 deg of rotation, the linear polarization of light was mostly lost due to scattering. Ambient light was blocked by a black, totally absorbing, paper tube. Light signals were detected by a sensitive charge coupled device camera (CCD-Camera) (Andor Corp., DV434, Belfast, Northern Ireland), which was thermoelectrically cooled down to -20°C . The CCD-Camera was equipped with a SIGMA 50 mm $f/2.8$ objective lens (SIGMA Corporation, Tokyo, Japan). A second polarizer (Hoya, Japan) was attached to the input of the lens and was adjusted either parallel or perpendicular to the polarization of the light used for

illumination. The whole experimental procedure was controlled with in-house-developed software, and images were stored on a PC.

2.2 Sample Preparation

The study involved patients presented at the Pigmented Skin Lesion Clinic of the University Hospital of Heraklion, Crete. All subjects were interviewed and underwent complete skin examination by the same two experienced dermatologists. Both benign and malignant melanocytic lesions (benign nevi, atypical nevi, melanomas) were included in the study. The lesions were totally excised and prepared in the Pigmented Skin Lesion Clinic in full accordance to the rules and guidelines of the Ethics Committee of the University Hospital and after approval of the Scientific Board of the University Hospital of Heraklion. The clinical investigations were conducted according to the Declaration of Helsinki Principles. Institutional approval and patient informed consent were obtained prior to undergoing the excision of the melanocytic lesion, after clinical and dermoscopic examination prior to the operation. The excision was performed under local anesthesia with a safety excision margin of healthy skin of 3 mm. The sizes of the excised samples ranged between 0.6 to 1.5 cm (as measured with a ruler). Excisional specimens were then placed into a sterile container, in a sterile splenium impregnated with physiological saline.

In the laboratory, the samples were fixated properly and then positioned on the rotation stage for the measurements. It must be noted that the samples were measured without optical clearing or other optical properties alteration treatment. At the end of the measurement, the samples were placed in plastic boxes filled with 10% buffered formalin, which is the commonly used tissue fixative and further processed to the surgical pathology laboratory for routine histological examination.⁴⁸ Between the excision, the optical-CT measurements and the histology, a maximum of 3% sample shrinkage is expected (in the order of 10s micrometers), therefore within the experimental error of our method.⁴⁹⁻⁵²

2.3 Measurements

The measurement process was initiated by positioning the samples in the center of rotation of the rotational stage and adjusted carefully so that off-center rotation is minimized. The stage was configured to rotate a full 360 deg with an image captured every 5 deg, corresponding with a total of 72 images and ensuring that the entire sample was illuminated and the transmitted light was

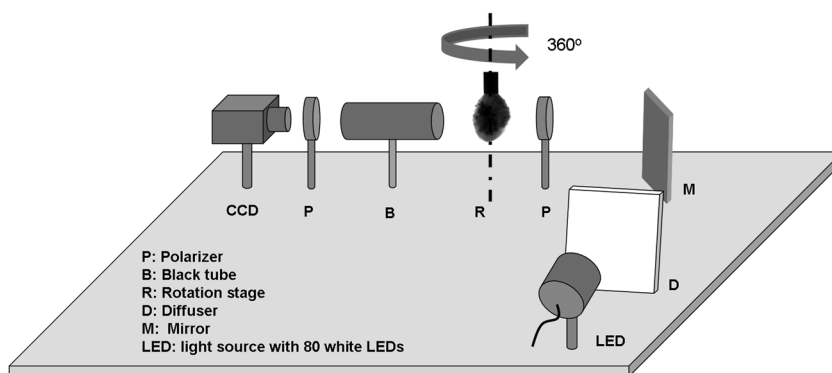


Fig. 1 Schematic representation of the optical-CT setup (LED: light-emitting diode; CCD: charge coupled device).

detected from several angles. These measurements were consistent throughout the entire study. The whole process was handled by in-house-developed software, which controlled and synchronized the CCD-Camera acquisition with the stepping of the rotation stage.

The first set of measurements consisted of white light images of the sample in all projections, followed by acquiring a background image without illumination for capturing any ambient light and background noise present in the measurements.

An important feature of the experimental setup was the combined use of the two polarizers, which allowed for selecting light transmitted either through or around the sample, depending on the relative position of their polarization axis. When the polarizers were crossed, light that has been transmitted through the sample and has lost its polarization due to scattering was detected. In contrast with that, when the polarizers were in parallel, light that has been transmitted around the sample and has maintained its polarization was detected.

The whole procedure was as follows: the polarizer located after the flat mirror was fixed in a constant position, providing the linear polarization of the incident light, while the polarizer mounted on the objective lens was adjusted according to the desired polarization of the transmitted light. A full set of measurements was acquired for both parallel and perpendicular positions, with the sample rotated in full 360 deg while illuminated constantly by the LED lamp. The measurements with the sample provided the transmitted light intensity, which corresponds with the term I of Beer's-Lambert's law as shown in Eq. (1):

$$I = I_0 \exp(-\mu_t \cdot x). \quad (1)$$

At the end, the samples were removed from the device, and measurements of the reference light were taken. Thus the intensity of the illuminating light was measured without samples, which corresponds with the term I_0 of Eq. (1).

Light propagation in tissues can be modelled as composed of an exponentially decaying component in the original direction of propagation (what is usually termed the "reduced intensity") and of other orders of angular dependence for which the diffusion approximation would result in the first order. The decaying contribution of the reduced intensity, properly modelled includes the total attenuation coefficient (μ_t), for which scattering is represented by the reduced scattering coefficient thus, on average, taking into consideration the anisotropy of scattering in the forward and backward directions. For the samples considered in this study as a first approximation, we assumed only reduced intensity is measured, greatly aided by the fact that we employ a small aperture on the objective lens (acting as a pinhole) to restrict the diffuse contribution (or higher angular orders) to a minimum.

2.4 Data Analysis

After completion of the experimental procedure described above, the data were processed for extracting the tomographic images with in-house-developed software and analyzed as following.

The recorded images were cropped and rotated for extracting and reconstructing only relevant information. Then the center of rotation of the sample was defined by calculating the variance between opposite projections for various centers of rotations. In the optical configuration used in this study, image projections are represented as line integrals generated from multiple sources

that emit light along parallel rays in a certain direction. These rays are spaced 1 pixel unit apart. To reconstruct an axial image consecutive parallel ray image projections $I(x, \theta)$ are captured at different angles θ . These are transformed according to Beer's law to calculate the sums of attenuation coefficients of the sample according to the following equation:

$$\int_{\text{ray}} \mu_t(x, y) ds = -\log \left[\frac{I(x, \theta) - Bg(x)}{I_0(x, \theta) - Bg(x)} \right], \quad (2)$$

where $\mu_t(x, y)$ is the 2-D representation of the attenuation coefficient of the sample confined on a single axial plane (x, y) , ds is the element of length along the ray where integration is carried out, $I(x, \theta)$ is the measured light intensity of a row of pixels that is transmitted through the irradiated sample at a specific angle θ , and $I_0(x, \theta)$ is the corresponding measured light intensity that is detected in the absence of a sample at the same θ . The value of $Bg(x)$ is the dark count measurement acquired by a row of pixels with the CCD lens cap on. The angular sequence of the measured light intensities $I(x, \theta)$ from a row of pixels forms a sinogram that reconstructs the corresponding axial slice using standard filtered back projection algorithm (inverse Radon transform).^{39,43} This slice is the 2-D distribution of the attenuation coefficients of the sample $\mu_t(x, y)$. The Ram-Lak filter was applied for the filtered back projections.³⁹ Detailed description of the reconstruction algorithm can be found in Refs. 39, 40, 43, and 44. Image post-processing was performed with Image J (<http://rsbweb.nih.gov/ij>), and the final calculations of the recovered optical properties were obtained and plotted.

The tomographic reconstructions were imported as raw images, and the axial slices showing the largest depth of the lesions were chosen from the 3-D stack. Then horizontal lines demarcating the upper and lower surfaces of the sample were applied and a depth profile perpendicular to these lines was drawn. The dependence of the attenuation coefficient with depth was calculated as the mean value obtained from five independent depth profiles. Specifically, the values of the attenuation coefficient as a function of depth across the axial slice were plotted against depth and fitted with the following formula:

$$y = y_0 \cdot \exp(-bx) + c, \quad (3)$$

where y_0 is the highest value of the profile, c is the minimum, x is the depth, and $1/b$ is a specific depth/pixel and is used to characterize the samples according to the following formula:

$$\text{depth} = 1/b \cdot 0.0128[\text{cm}], \quad (4)$$

where 0.0128 is the pixel size.

In presenting the data, special care was taken so that the orientation of the reconstructions was very similar to the orientation of the histology images. The lesions were in the upper part of the reconstruction where the higher (whiter) values of attenuation coefficient were observed. The lines demarcating the boundaries of the lesions were drawn during histology and were as parallel to the surface as possible considering the individual shape of its tissue sample.

2.5 Histological Examination of the Samples

Each specimen was examined macroscopically by a pathologist, and the whole lesion was cut in serial slices 3 mm in thickness and embedded in one, two, or three paraffin blocks, depending

on its dimensions. The hematoxylin- and eosin-stained sections from each lesion were examined microscopically for the histologic diagnosis. Then the area with the maximum thickness of the lesion was selected and measured microscopically.

The depth of invasion for malignant melanomas was measured from the top of the granular layer to the deepest extension of the tumor; in ulcerated lesions, measurement was from the ulcer base overlying the deepest point of invasion.

The thickness of each melanocytic nevus was measured from the top of the granular layer of the epidermis to the deepest extension of the lesion.⁴⁸

2.6 Statistical Analysis

Comparisons of variable distributions between groups were performed using nonparametric statistics (Kruskal-Wallis test and Wilcoxon signed rank test). All P values calculated were two-sided and the significance level was chosen to be 0.05. The thickness of melanocytic lesions experimentally determined by optical-CT was plotted against the values assessed by histology.

The correlation between the two methods was highlighted by the slope and R^2 values of the linear fit. Additionally, the values obtained by the two different methods were compared by means of a Wilcoxon signed rank test. All calculations were performed with the Statistical Package for Social Sciences (SPSS) version 17.0.

3 Results

The study was carried out on a total of 16 samples, divided as follows: six samples were identified as malignant melanomas of the skin, four as dysplastic melanocytic nevi, and six were histologically characterized as nondysplastic melanocytic nevi (however, these had been characterized clinically and dermoscopically as atypical). One common nevus, one hemangioma, and normal skin were used as controls. The highest values of the AC obtained from the fits described in Sec. 2.4 for each sample are presented in Table 1.

In Fig. 2, three characteristic melanocytic lesions are presented: one nondysplastic nevus (2.1), one dysplastic nevus

Table 1 Highest attenuation coefficient of different melanocytic lesions and their estimated thickness assessed by LED optical tomography and conventional pathological examination. The values were rounded to the closest significant figure.

Type of lesion	HighestAC (cm^{-1})	AC estimated thickness (mm)	Histological thickness (mm)
non-DN	3,50	0,4	0,30
non-DN	3,09	0,4	0,40
non-DN	3,45	3,3	3,00
non-DN	3,46	1,0	1,10
non-DN	3,14	0,8	0,83
non-DN	3,52	0,6	0,50
DN	5,54	1,5	1,60
DN	5,67	0,7	0,76
DN	5,89	1,2	1,24
DN	5,59	0,7	0,70
CM	7,62	0,5	0,40
CM	7,36	0,2	0,20
CM	7,20	0,7	0,80
CM	7,72	0,6	0,58
CM	8,03	2,3	2,20
CM	8,06	1,7	1,69
Normal skin 1	0,46	–	–
Normal skin 2	0,55	–	–
Normal skin 3	0,51	–	–
Hemangioma	0,68	–	–
Common nevus	1,47	–	–

Note: AC: attenuation coefficient; DN: dysplastic nevus; CM: cutaneous melanoma.

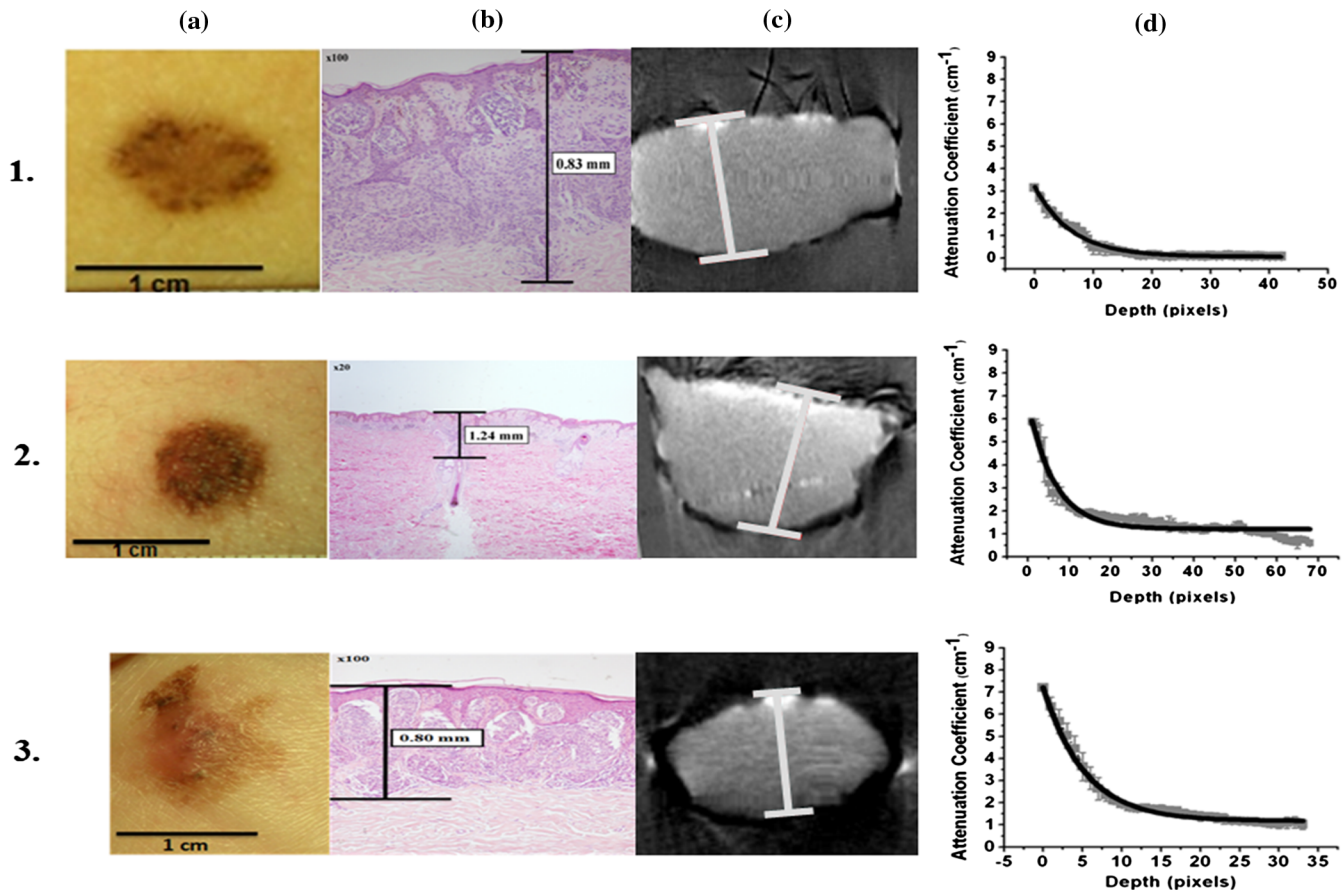


Fig. 2 Characteristic images of lesions from each studied group: (2.1) nondysplastic nevus; (2.2) dysplastic nevus; (2.3) melanoma. (a) Macroscopic image of the lesion. (b) Histological image of the lesion with measured depth. (c) Image of an axial slice obtained from the 3-D reconstructed image. The grey line shows the location of the profile. (d) Plot of the attenuation coefficient against depth obtained along the grey line of image 2C.

(2.2), and one melanoma (2.3). The images of columns A, B, C, and D correspond with simple white-light photographs, histological images, 3-D reconstructions, and AC plots as a function of depth, for the related samples. From the plots of the AC against depth, it is observed that the highest value obtained was $7.20 \pm 0.07 \text{ cm}^{-1}$, and it corresponded to melanoma (2.3.D). In the dysplastic nevus the highest AC value was $5.89 \pm 0.15 \text{ cm}^{-1}$ and in nondysplastic nevus $3.14 \pm 0.13 \text{ cm}^{-1}$. As shown also in Table 1, in which the findings for each lesion are presented, the highest AC values correspond with the malignant lesions, where morphological atypia of the cells and architectural disorder of the tissue are more intense. We attribute the increased AC to the higher scattering properties of dysplastic and malignant tissue. Hence this approach provides the ability to evaluate each pigmented skin lesion according to its cytological atypia, which is characteristic for its malignancy.

In Fig. 3, the plots of the attenuation coefficient against depth obtained from: (a) normal skin; (b) hemangioma; and (c) common nevus are presented. The plots in (d); (e); and (f) show the same profiles plotted with the scale of the graphs of Fig. 2 for a direct comparison. As can be noticed, the highest value of attenuation coefficient in these three plots is 1.47 cm^{-1} , and it is obtained in the common nevus. The corresponding value for hemangioma is 0.68 cm^{-1} and for normal skin 0.46 cm^{-1} . These three samples were used as controls of non-atypical tissue. The highest values of attenuation coefficient

in these samples are much lower than those in cutaneous melanomas, in dysplastic nevi, and even in nondysplastic nevi. This is due to the lower concentration of pigments, even for common nevus and to the fact that there is no morphological atypia of the cells and architectural disorder of the tissue. Therefore, the attenuation coefficient values are very low, and these samples can be easily differentiated from atypical or malignant lesions. This constitutes a confirmation of our results and our suggestions, whereas samples of normal skin or benign lesions of the skin have low values of AC and can be easily evaluated and discriminated from atypical and malignant pigmented skin lesions.

Determination of the thickness of cutaneous melanoma is important for assessment of further therapy of the pathological condition. Figure 4 depicts the effective depth calculated with the fitting process described in Sec. 2.4, plotted against the thickness provided by standard pathological assessment for each sample. The data were fitted with a linear formula with an R^2 value of 0.987, highlighting the excellent agreement of the optical-CT and histology results. No statistically significant difference was observed when thickness values obtained by optical-CT were compared with histological thickness using a Wilcoxon signed rank test ($P = 0.243$). The absolute difference of histological thickness minus AC estimated thickness ranged from 0.02 to 0.30 mm (median: 0.05 mm), exceeding 0.1 mm only in one sample (No. 3, see Table 1). The assessment of this thickness determines the prognosis and the selection of

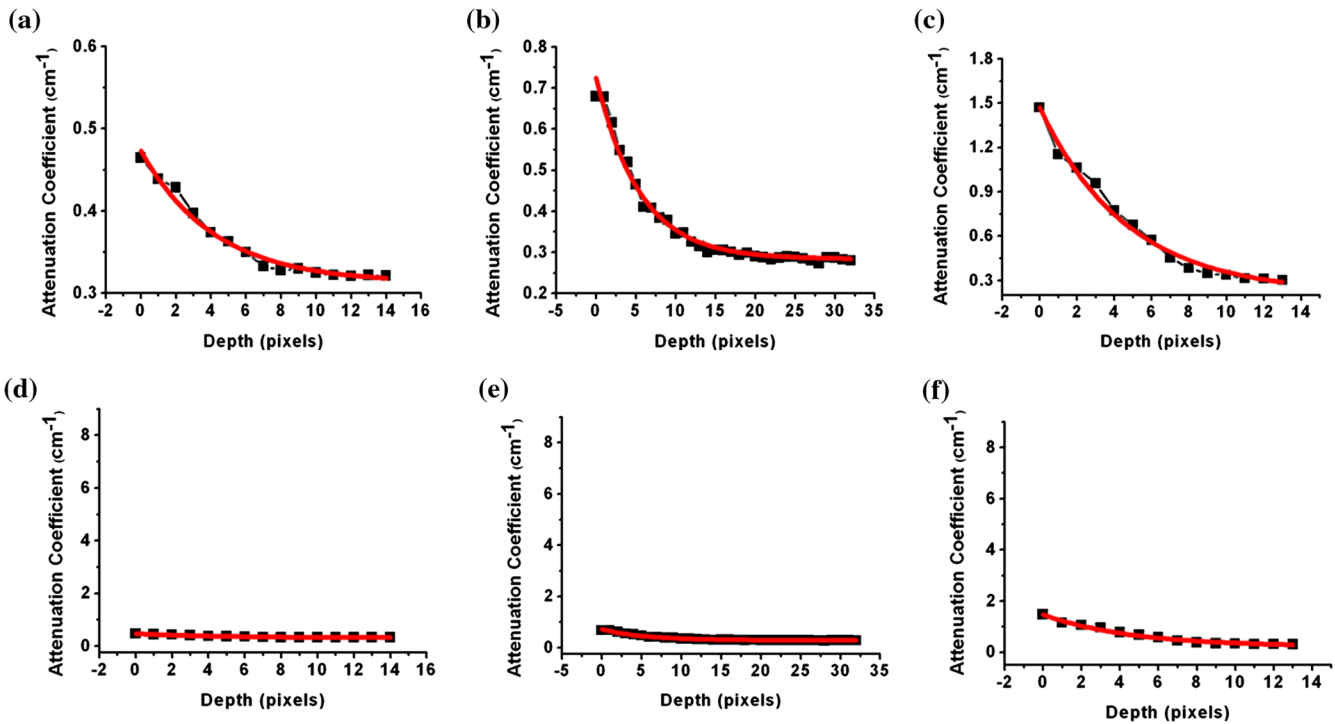


Fig. 3 Plots of the attenuation coefficient against depth obtained from: (a) normal skin; (b) hemangioma; and (c) common nevus. The plots in (d), (e), and (f) show the same profiles plotted with the scale of the graphs of Fig. 2 for a direct comparison.

the optimal treatment, which is important for the physician, assisting him in a much shorter time than histology to decide and choose the most favorable management of melanoma.⁴⁵ At this point we need to emphasize that the investigation was doubly blind, meaning that the involved parties had no information regarding the results from each other.

Finally, as presented in Fig. 5, there was a statistically significant difference of highest AC values between malignant melanomas, dysplastic nevi, and nondysplastic nevi as indicated by Kruskal-Wallis test ($P = 0.001$). Median (range) AC values were higher for malignant melanomas compared with dysplastic and nondysplastic nevi [7.67(0.86) vs. 5.63(0.35) vs. 3.45(2.05), respectively]. The range of the value for the nondysplastic nevi appears to be higher only because we have included in this category the one common nevus sample, the value of which is

presented by the asterisk in the graph of Fig. 5. These results suggest that optical-CT can be employed for the characterization and differentiation of pigmented skin lesions and assist the immediate evaluation of biopsy samples, based on the 3-D reconstructed maps of the total attenuation coefficient.

4 Discussion

In this paper we have demonstrated that optical-CT can be a valuable tool for imaging and characterization of biopsy samples of melanocytic tumors. Our study provides preliminary evidence that the 3-D maps of attenuation coefficient as provided by optical-CT may be used for the classification of common nevi, dysplastic nevi and cutaneous melanoma, as well as for

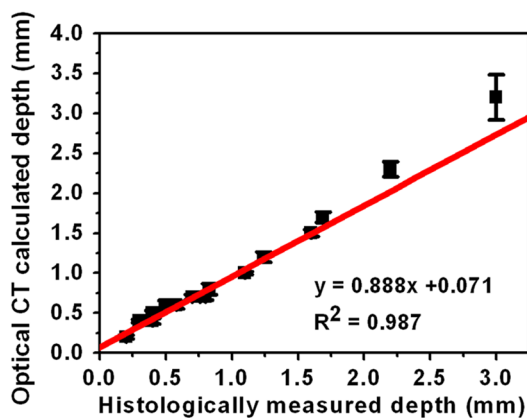


Fig. 4 Thickness estimated with the use of attenuation coefficient (AC) plotted against thickness provided by standard pathological assessment for each sample.

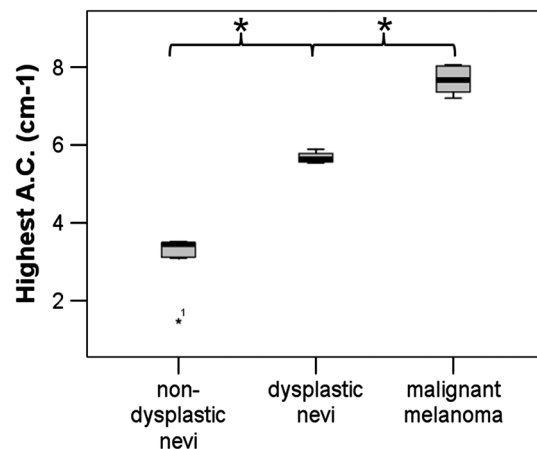


Fig. 5 Box plot of highest values of attenuation coefficient (AC) for each group of lesions ($P < 0.01$). The asterisk represents the value of the one common nevus sample.

the evaluation of the maximum thickness including Breslow thickness for melanomas.

The diagnostic accuracy of melanocytic lesions is an important factor for the prognosis and therapeutic interventions of skin cancer. This has created the need for the development of imaging methods such as *in vivo* confocal laser scanning microscopy,^{16–25} high-resolution ultrasound (U/S),^{26–29} spectroscopy,^{30–33} and OCT.^{29,34–37} However, none of them to date has been established in the diagnosis of melanoma.

OCT is an imaging modality, which provides high-resolution cross-sectional images. OCT is equivalent to confocal microscopy but with an added coherence gate, which decreases the noise floor. For both techniques, the contrast mechanism is backscattered light reflection. Similarly, ultrasound imaging uses backscattered sound waves for detecting the echo reflected from different tissue layers. It is a method that has been used to visualize and characterize melanocytic skin lesions. Related studies detected significant differences between benign nevi and malignant melanomas and suggested features that may serve in differentiation of melanocytic lesions. Although OCT appeared as a promising noninvasive imaging technique for the micromorphology of the skin, it has not been studied systematically in malignant melanoma (MM), and its major limitation is penetration depth, which cannot exceed 1 mm.^{29,34–37}

Recently, second harmonic generation has been demonstrated for imaging the collagen on skin lesions and determining melanoma borders, based on collagen morphology and density. However, despite the high sophistication of the technique, it did not offer detailed and accurate evidence for the discrimination of the malignant from benign melanocytic lesions, yet.³⁸

In this work we have chosen to explore the capabilities of optical-CT with in-house-developed system using white-light illumination with LEDs, due to the 3-D attenuation maps it can deliver. A diffused light illumination pattern was preferred exploiting 80 white LED lights, to achieve a uniform irradiation of the whole sample. A rotation stage with a purpose build sample holder was used to cover 360 deg of rotation, with a CCD capturing images every 5 deg, ensuring that the entire sample was illuminated and transmitted light signals were detected from several angles. An important feature of the system was the use of two polarizers, enabling to distinguish between light transmitted through or around the samples. This resulted in an increase in sensitivity and dynamic range of scattered light detection and allowed the imaging of thick biopsy samples. In this study only the perpendicular polarization measurements were used to reconstruct the 3-D image for each sample. The parallel polarization could instead be used for reconstructing the surface boundaries of the sample and for separating scattering from absorption using the radiative transfer equation with appropriate phase functions such as the Rayleigh phase matrix.^{53,54} Our initial experiments were accomplished *ex vivo*, as an optical 3-D histology, in order to evaluate different types of tissue and study the light transport through macroscopic samples. In the initial investigations a simple back-projection reconstruction algorithm provided the 3-D map of the attenuation coefficient, which enabled us to evaluate the melanocytic lesions in their whole thickness.

The optical-CT reconstructions provide 3-D maps of the total attenuation coefficient inside the biopsy samples, which correspond with the sum of absorption and scattering coefficients.

Absorption in the samples investigated can be mainly attributed to melanin, which is the main absorber of melanocytic lesions. Thus the reconstruction provides an image of the differences in the distribution and quantity of melanin at different areas of the tissue. However, the variation in measured optical properties between nevi and melanoma may not be totally explained by differences in the melanin content of the lesions, as melanin content may be similar in different types of melanocytic lesions. An important difference between benign and malignant lesions is attributed to the morphological atypia of the cells and architectural disorder of the tissue of the malignant lesions, which can influence (increase) light scattering, thus affecting the total attenuation coefficient, on which our results are based. Hence a higher total attenuation coefficient can be expected from the malignant lesions, which is what we have also measured with our optical-CT system. The ability to discriminate benign from malignant melanocytic lesions is thus based on the differences in the measured attenuation coefficient in different types of melanocytic lesions, which depend on the atypia of cancer cells. In addition, the different values of attenuation coefficient in different tissues, as well as in different cells, concerning their morphological formality offer us the ability to detect the boundary of the lesion and determine the thickness of invasive melanoma.

At this point it must be noted that although our study provided remarkably accurate results, it has been performed with a simple back projection algorithm, which does not account for light diffusion in tissue. This was compensated partially by the use of the diffuser and the polarizers, as described in detail in the Sec. 2. We are, however, researching the development of algorithms that use the diffusion theory for the reconstructions and will be able to dynamically adjust the phase function, which describes the scattering. These approaches include:

1. The use of wider weight functions in our simple back projection algorithm as described in a previous publication.⁵⁵ Going from a pencil-like to a diamond-shaped weight function provides a wider light propagation model.
2. Development of a theoretical approximation to the radiative transfer equation (RTE) that will fit the coexistence of weakly scattering, single scattering, and multiple scattering regions in the media. Building and testing of a hybrid reconstruction method for absorption inside those media where the scattering has been taken into account. Based on an initial separation of the media into weakly and highly scattering regions accommodates for calculation of light propagation for ballistic and diffusive regions. Study of the interfacing conditions between the highly scattering and weakly scattering regions.
3. Study of the effect of refractive index variation in the propagation of light through the weakly scattering medium with high scattering inclusions. Inclusion of refractive index variation in the forward model using the necessary boundary conditions between the highly and weakly scattering regions. Assessment of the significance of refractive index variation for the quality and the resolution of the reconstruction against the computational effort that it will require.

Furthermore, sensitivity and specificity studies including other skin tumors [basal cell carcinoma (BCC); squamous cell carcinoma (SCC)] except the melanocytic lesions described in this paper are under way.

Provided that the results of the current study will be confirmed by larger scale studies then optical-CT might allow for an immediate examination of the biopsies, ideally assisting the physician to have a direct classification of the lesion along with an evaluation of its thickness in a much shorter time than via histology. The assessment of this thickness can determine the prognosis and the selection of the most favorable management of melanoma.⁴⁵ This will lead to lower cost for the health system and less inconvenience for the patient.

Acknowledgments

The authors acknowledge support from the FP7 Collaborative Project “Hybrid Fluorescence Molecular Tomography (FMT)—X-ray Computed Tomography (XCT) method and system (FMT—XCT),” contract GA No. 201792.

References

1. J. Bauer and C. Garbe, “Acquired melanocytic nevi as risk factor for melanoma development. A comprehensive review of epidemiological data,” *Pigm. Cell Res.* **16**(3), 297–306 (2003).
2. C. Bosetti et al., “Mortality from cutaneous malignant melanoma in Europe. Has the epidemic leveled off?,” *Melanoma Res.* **14**(4), 301–309 (2004).
3. C. Garbe and U. Leiter, “Melanoma epidemiology and trends,” *Clin. Dermatol.* **27**(1), 3–9 (2009).
4. K. G. Lasithiotakis et al., “The incidence and mortality of cutaneous melanoma in southern Germany. Trends by anatomic site and pathologic characteristics, 1976 to 2003,” *Cancer* **107**(6), 1331–1339 (2006).
5. C. M. Balch et al., “An evidence-based staging system for cutaneous melanoma,” *CA Cancer J. Clin.* **54**(3), 131–149 (2004).
6. D. E. Elder et al., “Dysplastic nevus syndrome: a phenotypic association of sporadic cutaneous melanoma,” *Cancer* **46**(8), 1787–1794 (1980).
7. D. E. Elder, “Dysplastic naevi: an update,” *Histopathology* **56**(1), 112–120 (2010).
8. M. H. Greene et al., “Precursor naevi in cutaneous malignant melanoma: a proposed nomenclature,” [letter] *Lancet* **316**(8202), 1024 (1980).
9. R. U. Peter, W. I. Worret, and J. Nickolay-Kiesthardt, “Prevalence of dysplastic nevi in healthy young men,” *Int. J. Dermatol.* **31**(5), 327–330 (1992).
10. J. M. Tripp et al., “Management of dysplastic nevi: a survey of fellows of the American Academy of Dermatology,” *J. Am. Acad. Dermatol.* **46**(5), 674–682 (2002).
11. I. H. Wolf et al., “Sensitivity in the clinical diagnosis of malignant melanoma,” *Melanoma Res.* **8**(5), 425–429 (1998).
12. K. Hoffmann et al., “Diagnostic and neural analysis of skin cancer (DANAOS): a multicenter study for collection and computer-aided analysis of data from pigmented skin lesions using digital dermoscopy,” *Br. J. Dermatol.* **149**(4), 801–809 (2003).
13. H. Kittler et al., “Diagnostic accuracy of dermoscopy,” *Lancet Oncol.* **3**(3), 159–165 (2002).
14. J. Mayer, “Systematic review of the diagnostic accuracy of dermoscopy in detecting malignant melanoma,” *Med. J. Aust.* **167**(4), 206–210 (1997).
15. M. E. Vestergaard et al., “Dermoscopy compared with naked eye examination for the diagnosis of primary melanoma: a meta-analysis of studies performed in a clinical setting,” *Br. J. Dermatol.* **159**(3), 669–676 (2008).
16. R. G. Langley et al., “*In vivo* confocal scanning laser microscopy of benign lentiginos: comparison to conventional histology and *in vivo* characteristics of lentigo maligna,” *J. Am. Acad. Dermatol.* **55**(1), 88–97 (2006).
17. A. Scope et al., “*In vivo* reflectance confocal microscopy of shave biopsy wounds: feasibility of intraoperative mapping of cancer margins,” *Br. J. Dermatol.* **163**(6), 1218–1228 (2010).
18. L. Bergfeld et al., “Quantitative and three-dimensional analysis of Langerhans cells in basal cell carcinoma. A comparative study using light microscopy and confocal laser scanning microscopy,” *Br. J. Dermatol.* **130**(3), 273–280 (1994).
19. G. Pellacani, A. M. Cesinaro, and S. Seidenari, “Reflectance-mode confocal microscopy of pigmented skin lesions improvement in melanoma diagnostic specificity,” *J. Am. Acad. Dermatol.* **53**(6), 979–985 (2005).
20. M. Rajadhyaksha et al., “*In vivo* confocal scanning laser microscopy of human skin: melanin provides strong contrast,” *J. Invest. Dermatol.* **104**(6), 946–952 (1995).
21. A. Gerger et al., “*In vivo* confocal laser scanning microscopy of melanocytic skin tumors: diagnostic applicability using unselected tumor images,” *Br. J. Dermatol.* **158**(2), 329–333 (2008).
22. C. Longo et al., “Confocal microscopy of recurrent naevi and recurrent melanomas: a retrospective morphological study,” *Br. J. Dermatol.* **165**(1), 61–68 (2011).
23. A. Gerger et al., “*In vivo* confocal laser scanning microscopy in the diagnosis of melanocytic skin tumors,” *Br. J. Dermatol.* **160**(3), 475–481 (2009).
24. V. Ahlgrimm-Siess et al., “*In vivo* confocal scanning laser microscopy of common naevi with globular, homogeneous and reticular pattern in dermoscopy,” *Br. J. Dermatol.* **158**(5), 1000–1007 (2008).
25. C. S. Chen et al., “Multimodal *in vivo* optical imaging, including confocal microscopy, facilitates presurgical margin mapping for clinically complex lentigo maligna melanoma,” *Br. J. Dermatol.* **153**(5), 1031–1036 (2005).
26. T. Gambichler et al., “Preoperative ultrasonic assessment of thin melanocytic skin lesions using a 100-MHz ultrasound transducer: a comparative study,” *Dermatol. Surg.* **33**(7), 818–824 (2007).
27. P. Guitera et al., “Melanoma histological Breslow thickness predicted by 75-MHz ultrasonography,” *Br. J. Dermatol.* **159**(2), 364–369 (2008).
28. C. C. Harland et al., “Differentiation of common benign pigmented skin lesions from melanoma by high-resolution ultrasound,” *Br. J. Dermatol.* **143**(2), 281–289 (2000).
29. M. Mogensen et al., “*In vivo* thickness measurement of basal cell carcinoma and actinic keratosis with optical coherence tomography and 20-MHz ultrasound,” *Br. J. Dermatol.* **160**(5), 1026–1033 (2009).
30. T. Durduran et al., “Bulk optical properties of healthy female breast tissue,” *Phys. Med. Biol.* **47**(16), 2847–2861 (2002).
31. A. Garofalakis et al., “Characterization of the reduced scattering coefficient for optically thin samples: theory and experiments,” *J. Opt. A: Pure Appl. Opt.* **6**(7), 725–735 (2004).
32. M. Moncrieff et al., “Spectrophotometric intracutaneous analysis: a new technique for imaging pigmented skin lesions,” *Br. J. Dermatol.* **146**(3), 448–457 (2002).
33. A. Torricelli et al., “*In vivo* optical characterization of human tissues from 610 to 1010 nm by time-resolved reflectance spectroscopy,” *Phys. Med. Biol.* **46**(8), 2227–2237 (2001).
34. J. G. Fujimoto et al., “Optical coherence tomography: an emerging technology for biomedical imaging and optical biopsy,” *Neoplasia* **2**(1–2), 9–25 (2000).
35. T. Gambichler et al., “Characterization of benign and malignant melanocytic skin lesions using optical coherence tomography *in vivo*,” *J. Am. Acad. Dermatol.* **57**(4), 629–637 (2007).
36. J. Welzel et al., “Changes in function and morphology of normal human skin: evaluation using optical coherence tomography,” *Br. J. Dermatol.* **150**(2), 220–225 (2004).
37. M. Mogensen et al., “Nail thickness measurements using optical coherence tomography and 20-MHz ultrasonography,” *Br. J. Dermatol.* **157**(5), 894–900 (2007).
38. C. Thrasivoulou et al., “Optical delineation of human malignant melanoma using second harmonic imaging of collagen,” *Biomed. Opt. Ex.* **2**(5), 1282–1295 (2011).
39. C. Kak and M. Slaney, *Principles of Computerized Tomographic Imaging*, IEEE Press, New York (1988).
40. S. R. Arridge, “Optical tomography in medical imaging,” *Inverse Probl.* **15**(2), R41–R93 (1999).
41. J. Ripoll and V. Ntziachristos, “Imaging scattering media from a distance: theory and applications of non-contact optical tomography,” *Mod. Phys. Lett. B.* **18**(28–29), 1403–1431 (2004).
42. M. Oldham et al., “Three-dimensional imaging of xenograft tumors using optical computed and emission tomography,” *Med. Phys.* **33**(9), 3193–3202 (2006).

43. A. E. Papadakis et al., "A new OCT apparatus for 3-D radiotherapy dosimetry: is free space scanning feasible?," *IEEE Trans. Med. Imag.* **29**(5), 1204–1212 (2010).
44. J. Sharpe et al., "Optical projection tomography as a tool for 3-D microscopy and gene expression studies," *Science* **296**(5567), 541–545 (2002).
45. D. J. Eedy, "Surgical treatment of melanoma," *Br. J. Dermatol.* **149**(1), 2–12 (2003).
46. H. Meyer et al., "Optical projection tomography for *in vivo* imaging of *drosophila melanogaster*," *Microsc. Anal.* **22**(5), 19–22 (2008).
47. A. E. Papadakis et al., "Technical note: a fast laser-based optical-CT scanner for three-dimensional radiation dosimetry," *Med. Phys.* **38**(2), 830–835 (2011).
48. J. Rosai and L. V. Ackerman, *Rosai and Ackerman's Surgical Pathology*, 10th ed., , Vol. 2, Elsevier Mosby, Edinburgh (2011).
49. H. C. Fox et al., "Formaldehyde fixation," *J. Histochem. Cytochem.* **33**(8), 845–853 (1985).
50. P. K. Hsu et al., "Effect of formalin fixation on tumor size determination in stage I non-small cell lung cancer," *Ann. Thorac. Surg.* **84**(6), 1825–1829 (2007).
51. J. N. Dauendorffer et al., "Shrinkage of skin excision specimens: formalin fixation is not the culprit," *Br. J. Dermatol.* **160**(4), 810–814 (2009).
52. M. J. Kerns et al., "Shrinkage of cutaneous specimens: formalin or other factors involved?," *J. Cutan. Pathol.* **35**(12), 1093–1096 (2008).
53. N. Ghosh, M. F. G. Wood, and I. A. Vitkin, "Mueller matrix decomposition for extraction of individual polarization parameters from complex turbid media exhibiting multiple scattering, optical activity, and linear birefringence," *J. Biomed. Opt.* **13**(4), 044036 (2008).
54. M. Ahmad et al., "Do different turbid media with matched bulk optical properties also exhibit similar polarization properties?," *Biomed. Opt. Ex.* **2**(12), 3248–3258 (2011).
55. G. M. Turner et al., "Complete-angle projection diffuse optical tomography by use of early photons," *Opt. Lett.* **30**(4), 409–411 (2005).